RAPID COMMUNICATIONS

PHYSICAL REVIEW B **81**, 100101(R) (2010)

Atomic-resolution chemical mapping using energy-dispersive x-ray spectroscopy

A. J. D'Alfonso,[1] B. Freitag,[2] D. Klenov,[2] and L. J. Allen[1]
[1]*School of Physics, University of Melbourne, Parkville, Victoria 3010, Australia*
[2]*FEI Company, Building AAE, Achtseweg Noord 5, Eindhoven, The Netherlands*

(Received 16 July 2009; revised manuscript received 19 September 2009; published 8 March 2010)

We demonstrate atomic-resolution chemical mapping using energy-dispersive x-ray spectroscopy in scanning transmission electron microscopy. Theoretical simulations of the imaging process demonstrate that these images are directly interpretable. This is due to the fact that the effective ionization interaction is local and this is an incoherent mode of imaging.

DOI: 10.1103/PhysRevB.81.100101 PACS number(s): 61.05.jd, 68.37.Ma, 78.70.En

Since atomic-resolution electron energy-loss spectroscopy (EELS) in scanning transmission electron microscopy (STEM) was first demonstrated[1–3] the field has progressed rapidly. The implementation of aberration correction in the electron optics has allowed probe sizes to approach less than 0.1 nm and this, coupled to increases in the EELS detector efficiency, has allowed chemical mapping of crystals in two dimensions.[4–7] Such maps are not always directly interpretable.[4] Muller and co-workers suggested that direct interpretability would be ensured provided a large EELS collection aperture was used, as was the case in their experiment using a new Nion UltraSTEM system in which detector angles as large as 60 mrad are feasible.[6] However, using a similar system installed in Daresbury, Wang *et al.*[7] obtained a contrast reversal when images were constructed for a similarly large detector acceptance angle but from differing regions of the energy-loss spectra. In principle, the difficulties of interpreting such anomalous results can be offset somewhat by simultaneously acquiring high-angle annular dark-field (HAADF) images to correlate the crystal structure with the corresponding EELS images.[8,9] However, for crystals containing light elements or species of similar atomic number, atom discrimination based on HAADF image contrast is difficult. Here, we demonstrate a complementary approach to chemical mapping that offers the direct visual interpretability of HAADF imaging, while simultaneously unambiguously identifying the atoms.

Energy-dispersive x-ray spectroscopy (EDS) in STEM has been used to map regions containing a particular species of atom in nanostructures.[10–12] In this method a coherent focused probe is raster scanned across the specimen and at each probe position the resultant x-ray emission spectrum is recorded. This spectrum is then used to construct an elemental map. Two advantages that STEM EDS has are that the inelastic interaction is always effectively local, like that in HAADF, and that the inner-shell ionization potential is as localized as possible for a given ionization edge. Consequently, the resulting incoherent image can be directly interpreted. In this Rapid Communication we show atomic-resolution chemical mapping based on STEM EDS using a FEI Titan 80-300. Theory explains and detailed calculations verify the direct interpretability of these chemical maps.

This study used a test sample of ⟨001⟩ $SrTiO_3$ that was electropolished and chemically etched, creating an ultraclean surface. This was essential as it was observed that even a small amount of surface amorphization had a negative impact on the quality of the result. The sample thickness was estimated to be 100 nm and a specimen of this thickness was needed to ensure sufficient x-ray counting statistics. The 300 kV probe had a third-order spherical aberration coefficient $C_s = 1.2$ mm. The probe forming aperture semiangle was 9.6 mrad and the probe was underfocused by 560 Å into the specimen. The probe size was estimated at 1.4 Å and the beam current was 10–20 pA. The EDS detector subtended a collection angle of 0.13 sr. The acquisition time for a single x-ray spectrum was 500 ms (corrected for dead time).

Two-dimensional chemical maps are shown in Fig. 1. That for the Ti sublattice is shown in Fig. 1(a), and that for the Sr sublattice is shown in Fig. 1(b). Shown in Fig. 1(c) is the simultaneously acquired STEM HAADF image. In each case the experimental EDS maps and the HAADF image have the simulations overlayed. Good qualitative agreement is seen and there is a one-to-one correspondence between the known projected structure, the EDS maps, and the HAADF image. The simulations will be discussed in more detail shortly.

Figure 2(a) shows a HAADF line scan along ⟨110⟩ and Fig. 2(b) shows the simultaneously recorded EDS line scans. The EDS line scans shown in Fig. 2(b) are consistent with the HAADF image in Fig. 2(a). These were extracted from the two-dimensional maps in Fig. 1. The Sr signal follows the reference HAADF line scan and this is to be expected as the HAADF contrast should be dominated by the Sr columns. The Sr line scan in Fig. 2(b) was constructed from the sum of the Sr *K*- and *L*-shell ionization events. The corresponding Ti line scan only uses the Ti *K* shell. The alternating Sr-Ti-Sr structure is clearly seen in the two line scans in Fig. 2(b).

A typical EDS spectrum is shown in Fig. 2(c) and it is instructive to notice that while the count rates are quite low, so is the accompanying background. While the x-ray detector count statistics may be considered low, the peak-to-background (P/B) ratio is high. Next generation detectors will have count rates an order of magnitude larger than that used here, thus improving signal-to-noise ratios.[13] This is in contrast to EELS where low P/B ratios often demand the use of principal component analysis in conjunction with conventional power-law background subtraction to remove spectral noise and obtain usable spectra.[4,14] Typical P/B ratios in EELS are around 1:1 and can become even worse in composite materials with many different atomic species, where edges of the different elements contribute to the background

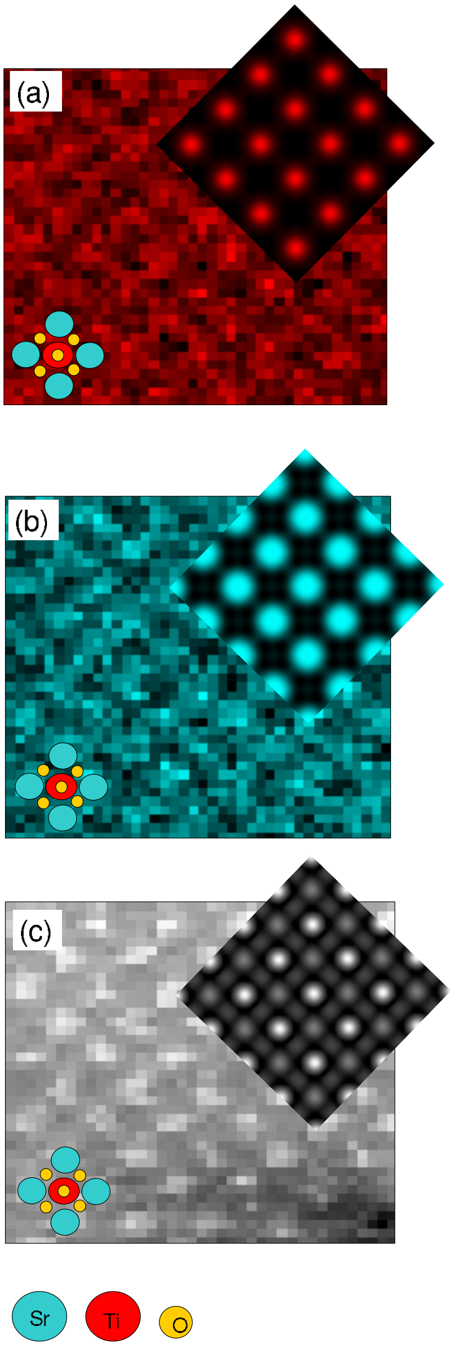

FIG. 1. (Color online) Experimental and simulated results (overlay) for $SrTiO_3$ chemical maps for (a) Ti and (b) Sr, and in (c) the corresponding STEM HAADF image. The sample was estimated to be 100 nm thick. The projected structure along the ⟨001⟩ direction is indicated on each map.

of the characteristic edges following at higher energy losses. For state-of-the-art EDS detectors P/B ratios of between 60:1 and 100:1 are possible depending on the energy loss of the characteristic absorption edge in the EDS spectrum.

It must be stressed that all of the data presented were obtained on a machine with no spherical aberration correction. Using multipole correctors will allow the illumination aperture to be increased, decreasing the probe wave-function spot size while simultaneously increasing the beam current.

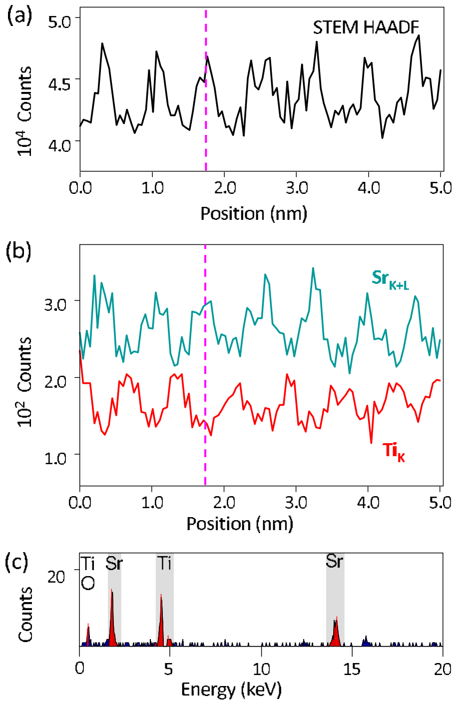

FIG. 2. (Color online) (a) Reference HAADF line scan of the $SrTiO_3$ sample along the ⟨110⟩ direction. The corresponding EDS line scans shown in (b) are for Ti and Sr and were constructed from the integrated shaded region of the x-ray spectrum indicated in (c), where a typical EDS spectrum is shown. The spectrum in (c) corresponds to the position indicated by the pink dashed lines in (a) and (b).

This would increase the beam density and in turn improve the x-ray yield per pixel and thus improve the quality of the chemical maps.[15]

The EDS simulations in Figs. 1(a) and 1(b) were performed following the formulation outlined in Ref. 16, which uses the frozen phonon algorithm[17–20] to also account for the contribution to the x-ray cross section from thermally scattered electrons. The effect of demagnifying the source to improve beam current and thus increasing the spatial incoherence of the probe has not been accounted for in any of the simulations. This may account for some discrepancies between the simulated and experimental images, but this does not affect our conclusions. The HAADF simulation in Fig. 1(c) was performed using the standard frozen phonon algorithm[20] for a HAADF collection range of 60–160 mrad. For the EDS maps the assumption is made that the total cross section for all x-ray emission events corresponding to filling a hole in the K or L shell is proportional to the total cross section for K- or L-shell ionization, respectively. For EELS imaging the angular range of the scattered electron integration would be limited to the physical dimensions of the EELS collection aperture. However, for EDS the integration extends over the full solid angle since electrons with all possible ionization scattering kinematics contribute to the signal. In that case the cross section for ionization as a function of the probe position $\boldsymbol{R}$ and the sample thickness t in the frozen phonon–mixed dynamical form factor (FPh-MDFF) synthesis is of the form

$$\sigma(\boldsymbol{R},t) = \frac{4\pi}{hvJ}\sum_{j=1}^{J}\int_0^t\int_A |\psi_j(\boldsymbol{R},\boldsymbol{r}_\perp,z)|^2 V(\boldsymbol{r}_\perp)d\boldsymbol{r}_\perp dz. \qquad (1)$$

Here, A is the incident area of the unit cell, J is the number of phonon configurations, $v=hk_0/m$ is the velocity of the incident electrons of mass m and wavelength $\lambda_0=1/k_0$, and ψ_j is the probe electron wave function for the jth frozen phonon configuration at a depth z. The effective local ionization potential $V(\boldsymbol{r}_\perp)$ is given in terms of transition potentials $H_{n0}(\boldsymbol{r}_\perp)$ as follows:

$$V(\boldsymbol{r}_\perp) = \frac{2\pi m}{h^2 t_c}\sum_n \frac{1}{k_n}|H_{n0}(\boldsymbol{r}_\perp)|^2, \qquad (2)$$

where t_c is the distance over which the potential is projected. The sum is in effect an integration over all possible final states (energies) of the ejected electron. These transition potentials become more localized as the energy of the ejected electron increases, i.e., for greater energy losses of the incident electron—see, for example, Ref. 7. Typically in EELS we integrate up over an energy-loss window on the order of 10 eV above the ionization threshold. The effective window in EDS is larger and the contribution of the final states with larger energy losses means that the potential in Eq. (2) becomes more localized about the atomic sites.

The form of Eq. (1) implies that EDS is an incoherent imaging mode akin to HAADF imaging and therefore is likely to deliver a one-to-one correspondence between image and structure. The effective scattering potentials for HAADF, Ti K-shell x-ray emission for EDS, and Sr K-plus L-shell x-ray emission are shown in Fig. 3. The HAADF potential is the most peaked and corresponds closely to the projected structure. It is more peaked around the Sr columns than on the Ti columns. The EDS potentials are also quite peaked and have a localization comparable to the HAADF potential. These potentials of course are pertinent to a particular atomic species in a sublattice. Examining Figs. 1(a) and 1(b) it is clearly evident that the Ti map is significantly more localized than the Sr map. This is a consequence of using the single tightly bound Ti K shell (threshold energy of around 4965 eV), as opposed to the sum of the relatively delocalized Sr L shell (threshold energy of around 2007 eV) with the Sr K shell. The relative full widths at half-maximum of the respective EDS potentials are 0.22 and 0.33 Å, respectively. The restriction to the Ti K shell is due to the relatively low energy resolution of the EDX detector and its inability to separately resolve the O K- and Ti L-shell events [as can be seen in Fig. 2(c)].

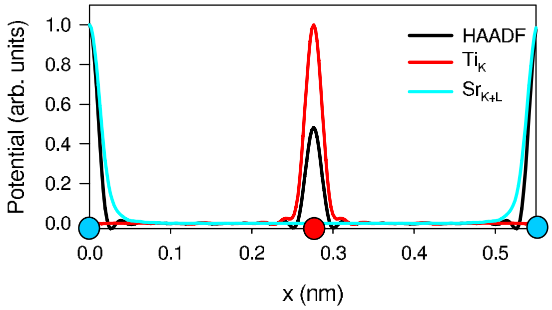

FIG. 3. (Color online) The effective scattering potential for HAADF for a detector spanning 60–160 mrad, Ti K-shell x-ray emission and the sum of the Sr K- and L-shell potentials for x-ray emission EDS. The scattering potential is for the ⟨110⟩ direction for a single unit cell of $SrTiO_3$. The Sr and Ti sites are indicated by the circles. For ease of comparison, each line plot has its maximum value normalized to 1.

In chemical mapping based on EELS a power-law subtraction is needed to remove an often substantial background from the ionization edge under consideration. Kimoto *et al.*[21] used the background extrapolation technique to extract spectra far from the edge onset to improve the spatial resolution of experimental EELS images, as it is well known that the degree of localization increases with increasing energy loss.[7,22] However, the further from the edge onset the more the accuracy of the extrapolation is tested. By contrast, in EDS all energy losses above the edge contribute to the signal while at the same time there is no substantial background subtraction to complicate the integration of the signal.

In summary, we have demonstrated two-dimensional atomic-resolution EDS chemical mapping in STEM. Theoretical simulations support the data and show why the maps are directly interpretable. The combination of simultaneous STEM EELS, HAADF, and EDS provides a powerful approach to investigate structural chemical and functional information in real space at the atomic resolution.

L.J.A. acknowledges support from the Australian Research Council. We thank Scott Findlay and Mark Oxley for helpful discussions.

---

[1] N. D. Browning, M. F. Chisholm, and S. J. Pennycook, Nature (London) **366**, 143 (1993); **444**, 235 (2006).

[2] D. A. Muller, Y. Tzou, R. Raj, and J. Silcox, Nature (London) **366**, 725 (1993).

[3] P. E. Batson, Nature (London) **366**, 727 (1993).

[4] M. Bosman, V. J. Keast, J. L. Garcia-Munoz, A. J. D'Alfonso, S. D. Findlay, and L. J. Allen, Phys. Rev. Lett. **99**, 086102 (2007).

[5] K. Kimoto, T. Asaka, T. Nagai, M. Saito, Y. Matsui, and K. Ishizuka, Nature (London) **450**, 702 (2007).

[6] D. A. Muller, L. Fitting Kourkoutis, M. Murfitt, J. H. Song, H. Y. Hwang, J. Silcox, N. Dellby, and O. L. Krivanek, Science **319**, 1073 (2008).

[7] P. Wang, A. J. D'Alfonso, S. D. Findlay, L. J. Allen, and A. L. Bleloch, Phys. Rev. Lett. **101**, 236102 (2008).

[8] M. Varela *et al.*, Phys. Rev. Lett. **92**, 095502 (2004).

[9] M. P. Oxley, M. Varela, T. J. Pennycook, K. van Benthem, S. D. Findlay, A. J. D'Alfonso, L. J. Allen, and S. J. Pennycook, Phys. Rev. B **76**, 064303 (2007).

[10] D. I. Enache, J. K. Edwards, P. Landon, B. Solsona-Espriu, A. F. Carley, A. A. Herzing, M. Watanabe, C. J. Kiely, D. W. Knight, and G. J. Hutchings, Science **311**, 362 (2006).

[11] A. A. Herzing, M. Watanabe, J. K. Edwards, M. Conte, Z.-R. Tang, G. J. Hutchings, and C. J. Kiely, Faraday Discuss. **138**, 337 (2008).

[12] D. B. Williams, A. J. Papworth, and M. Watanabe, J. Electron Microsc. **51**, S113 (2002).

[13] H. S. von Harrach, P. Dona, B. Freitag, A. Niculae, and M. Rohde, Microsc. Microanal. **15**, 208 (2009).

[14] N. Bonnet, N. Brun, and C. Colliex, Ultramicroscopy **77**, 97 (1999).

[15] M. Watanabe, D. W. Ackland, A. Burrows, C. J. Kiely, D. B. Williams, O. L. Krivanek, N. Dellby, M. F. Murfitt, and Z. Szilagyi, Microsc. Microanal. **12**, 515 (2006).

[16] S. D. Findlay, M. P. Oxley, S. J. Pennycook, and L. J. Allen, Ultramicroscopy **104**, 126 (2005).

[17] S. Hillyard, R. F. Loane, and J. Silcox, Ultramicroscopy **49**, 14 (1993).

[18] R. F. Loane, P. Xu, and J. Silcox, Ultramicroscopy **40**, 121 (1992).

[19] R. F. Loane, P. Xu, and J. Silcox, Acta Crystallogr., Sect. A: Found. Crystallogr. **47**, 267 (1991).

[20] E. J. Kirkland, *Advanced Computing in Electron Microscopy* (Plenum Press, New York, 1998).

[21] K. Kimoto, K. Ishizuka, and Y. Matsui, Micron **39**, 257 (2008).

[22] R. F. Egerton, *Electron Energy-Loss Spectroscopy in the Electron Microscope* (Plenum Press, New York, 1996).